

Effects of Nucleus Density and Dendritic Growth Influenced by Ti and Nb on Solidification Structure of Fe-18 Pct Cr Ferritic Stainless Steel



YUYANG HOU and GUO GUANG CHENG

The effects of nucleus density and dendritic growth influenced by Ti and Nb on the solidification structure of Fe-18 pct Cr ferritic stainless steel (FSS) ingots were investigated. The equiaxed zone ratios (EZR) were 8.5, 28.8, 67.5, and 57.3 pct in the blank, Nb-bearing, Ti-bearing, and Ti-Nb-bearing FSS ingots, respectively. The grain size was the smallest in the Ti-Nb-bearing ingot. Silicon oxide was present in the blank sample and Nb-bearing ingot, but the complex nuclei that were composed of $TiO_x-Ti(C, N)$ and $TiO_x-(Ti, Nb)_x(C, N)_y$ existed in the Ti-bearing and Ti-Nb-bearing ingots, respectively. The bulk density of the complex nucleus decreased by 70 pct when the Ti content decreased from 0.16 to 0.14 mass pct. Thermodynamic calculations indicate that the phase transformation from Ti_3O_5 to Ti_2O_3 was delayed in the ingot with a lower Ti content and that the Ti_2O_3 shows more potential for TiN nucleation compared with Ti_3O_5 according to the disregistry theory. The increased EZR mechanism was illustrated by a cellular-automaton–finite-element method with actual distribution statistics of the complex nucleus and dendritic-growth-kinetic analysis. The heterogeneous nucleation effect of the complex nucleus by Ti addition and the variations in dendritic-growth kinetics by Ti and Nb contribute to the EZR increase of FSS.

<https://doi.org/10.1007/s11663-019-01557-5>

© The Minerals, Metals & Materials Society and ASM International 2019

I. INTRODUCTION

FERRITIC stainless steel (FSS) is a nickel-saving stainless steel with a beneficial price advantage. Because of its special corrosion resistance, thermal conductivity, and other excellent properties, FSS has recently attracted increased attention. With reductions in carbon and nitrogen and the application of stabilizing elements, Ti and Nb, the FSS intergranular corrosion resistance has improved significantly. Ti and Nb dual-stabilized FSS has developed rapidly with extensive application prospects.

Ridging is a typical defect that occurs during deformation, affects the formability and surface quality, and restricts the application of FSS. It has been reported in numerous studies that the occurrence of ridging can be attributed to a high ratio of columnar crystals within the FSS as-cast structure.^[1–8] Therefore, a high equiaxed zone ratio (EZR) is expected to be obtained immediately after FSS solidification. Although the application of low-superheat casting, electromagnetic stirring has been

used to improve the EZR,^[9,10] an interruption in continuous casting and an increase in equipment and operating cost were encountered. The application of low-superheat casting and electromagnetic stirring provides limited benefits to increasing the EZR owing to the good dendritic-growth kinetics of the FSS.^[11]

Heterogeneous nucleation is considered an effective method to improve the EZR. Among these, the control of TiN formation was thought to be an effective way to promote heterogeneous nucleation. TiN decreases the nucleation undercooling, and has excellent lattice-matching properties with δ -Fe,^[12] which promotes the heterogeneous nucleation of δ -Fe. Itoh *et al.*^[13] found that Ti addition increases the EZR of an FSS slab regardless of the superheat of the molten steel. A higher EZR could be attributed to the heterogeneous nucleation effect of the Ti_2O_3 -TiN and $MgAl_2O_4$ -TiN complex nucleus that appeared in the as-cast ingot or slab when Ti was alloyed in FSS.^[14–16] However, the distribution and amounts of complex nuclei have a significant influence on the formation of equiaxed grains. Besides stabilization, most research that refers to Nb alloying focused on the performance of FSS in a high-temperature environment.^[17–19] Few studies have been conducted on the effect of elemental Nb on the EZR of Ti and Nb dual-stabilized FSS.

YUYANG HOU and GUO GUANG CHENG are with the State Key Laboratory of Advanced Metallurgy, University of Science and Technology Beijing, Beijing 100083, China. Contact e-mail: chengguo Guang@metall.ustb.edu.cn

Manuscript submitted November 9, 2018.

Article published online March 22, 2019.

Many researchers have focused on the formation mechanisms and compositional evolution of Ti-bearing oxide in the molten stage of FSS. The chemical composition can influence the nucleus density in FSS nucleation significantly, but this phenomenon has rarely been studied. In a previous study,^[11] the EZR was increased by slowing the dendritic growth of Fe-20 pct Cr FSS without introducing the heterogeneous nuclei. In terms of dendritic growth, relevant data are lacking, and theoretical models have not been established for Ti and Nb dual-stabilized FSS. The situation is complicated by the combined effect of nucleation and dendritic growth, which occurs commonly in Ti and Nb dual-stabilized FSS. The columnar-to-equiaxed transformation (CET) could occur when the nucleation capacity exceeds the growth trend of columnar grains.^[20,21] A fundamental understanding of the interactive behavior between the heterogeneous nucleation and dendritic growth is required for Fe-18 pct Cr FSS, which was investigated in this work experimentally, and by calculation and simulation.

II. EXPERIMENTAL

A vacuum-induction furnace was chosen to prepare a 5-kg experimental ingot. Raw materials of pure iron plate and chromium blocks were heated and melted in the furnace. When the raw material was melted, the temperature of the molten steel was increased rapidly and maintained at 1615 ± 15 °C for 10 minutes to dissolve the chromium metal into the molten steel. Nb pieces and titanium sponge were added sequentially to the molten steel under vacuum after deoxidation with silicon metal. The ingot was removed when the molten steel was solidified in a mold after casting and cooled in air to room temperature. Table I lists the average compositions of the four ingots. Ingot A is the blank sample, Ingot B is the test sample with 0.20 mass pct Nb, Ingot C has 0.16 mass pct Ti and Ingot D has 0.14 mass pct Ti and 0.21 mass pct Nb.

The ingots were in the shape of a 140-mm-high truncated cone, with a bottom and a top diameter of 60 and 80 mm, respectively. The outline dimensions of the ingot are shown in Figure 1. The ingots were cut vertically into two parts through the centerline. The as-cast structure was revealed on one part by etching using aqua regia solution ($\text{HCl}:\text{HNO}_3 = 3:1$). A metallographic sample was taken from another part for particle analysis. Except for the triangular region of the as-cast structure, the heat transfer in the ingot was concentrated mainly in the direction of the maximum temperature gradient, which was approximately one-dimensional in the steady state. For practical significance of the research results, the EZR measurement method is shown in the upper part of Figure 1.^[22]

The characteristics and composition of particles in the ingots were analyzed by means of a FEI Quanta scanning electron microscope with an energy-dispersive spectrometry (EDS) X-ray analyzer. FactSage (ThermoFact/CRCT, Montreal, Canada and GTT-Technologies,

Aachen, Germany) software^[23–25] was applied to analyze the formation and evolution of the oxide phases. Thermo-Calc (Thermo-Calc Software AB, Solna, Sweden) software^[26,27] was applied to analyze the precipitates and phase transformation during solidification. Differences in dendritic-growth kinetics of the four FSS ingots were investigated through a multicomponent model based on the Kurz–Giovanola–Trivedi model.^[11,28–31] The heterogeneous-nucleation particle density was determined from statistics of the effective nuclei. The kinetic and nuclei density tests were applied in a cellular-automaton–finite-element (CAFE) model^[32–35] to illustrate the evolution of solidification structure and to understand the CET of the dual-stabilized FSS. Dendritic growth modeling and the as-cast structure simulation have been described in detail in previous work.^[11] Through these methods, the heterogeneous-nucleation and dendritic growth features, and parameters for Ti and Nb dual-stabilized FSS were revealed and are discussed in this study.

III. RESULTS

A. As-cast Structure

The as-cast structures of the four experimental ingots are shown in Figure 2. The EZRs of ingots A, B, C, and D are 8.5, 28.8, 67.5, and 57.3 pct, respectively. The EZR increases obviously when Ti was added to Ingots C and D, compared with Ingots A and B. With Nb addition, the EZR increases slightly in Ingot B without Ti addition compared with Ingot A, but decreases slightly in Ingot D with Ti addition compared with Ingot C. In terms of solidification structure and composition, the EZR is higher in Ingot C with a higher Ti content when the elemental N is almost the same. However, when the Nb is alloyed, the grain size is finer, regardless of whether it contains equiaxed or columnar crystals. The characteristics and composition of particles in these ingots were analyzed to establish the influence of Ti and Nb alloying on the solidification structure of the FSS.

B. Particles in Ingots

The morphology and composition of particles in these ingots are shown in Figure 3. For Ingots A and B that were alloyed with no titanium, the major inclusions were spherical silicon oxide, and a small amount of Nb was present in the silicon oxide in Ingot B. Although they differed from Ingots A and B, the major inclusions in Ingots C and D were mainly Ti-bearing complex nuclei. The EDS results show that the central part of the complex nucleus was mainly TiO_x , which was enveloped by a $\text{Ti}(\text{C}, \text{N})$ layer in Ingot C and Ti or Nb-rich $(\text{Ti}, \text{Nb})_x(\text{C}, \text{N})_y$ layers in Ingot D. Particles changed significantly in Ti-containing Ingots C and D, accompanied by an obvious increase in EZR. The differences in Ti and Nb contents lead to changes in EZR, which were studied in detail.

Table I. Chemical Composition of the Four Ingots (Mass Percent)

Ingots	Cr	Ti	Nb	Al	Si	C	N	O
A	17.8	—	—	0.0038	0.48	0.0097	0.012	0.012
B	17.9	—	0.20	0.0052	0.50	0.0087	0.011	0.011
C	17.7	0.16	—	0.0066	0.46	0.0100	0.011	0.005
D	17.9	0.14	0.21	0.0045	0.49	0.0080	0.011	0.006

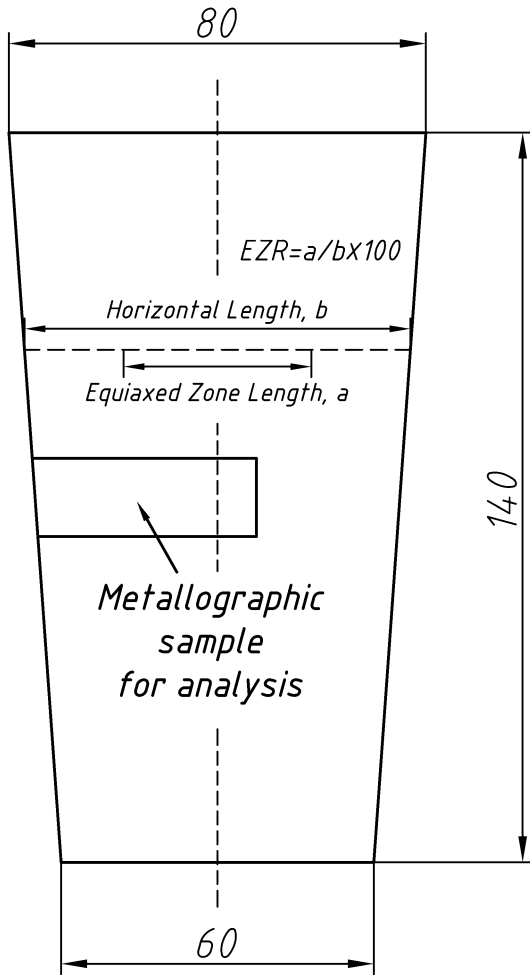


Fig. 1—Longitudinal section schematic of ingot and mold during solidification.

C. Particle-Size Distribution and Nuclei Density

The feature diameter (mm) distributions are shown as a histogram in Figure 4 after statistical analysis of complex nuclei. Figure 4(a) represents the Ti-bearing Ingot C, and Figure 4(b) shows the Ti- and Nb-bearing Ingot D. The horizontal coordinate represents the feature diameter of the complex nucleus with intervals of 0.25 μm; the vertical coordinate represents the percentage of the corresponding diameter in Figures 4(a) and (b). The average diameter of the complex nucleus in Ingot C is 1.67 μm and that in Ingot D is 1.42 μm. After statistical analysis, the bulk density of complex nucleus in Ingot C was $1.19 \times 10^{12} \text{ m}^{-3}$ and that of Ingot D was $3.18 \times 10^{11} \text{ m}^{-3}$. The particle-diameter distribution is

concentrated near the average particle diameter in Ingots C and D. According to research by Fu *et al.*,^[36] nearly 30 pct of total TiN can promote FSS nucleation, which was considered as the maximum-nuclei density percentage. In addition, another distribution peak appears in the particle diameter range of less than 0.5 μm, probably because of precipitation after solidification.

It can be concluded from Figure 4 that the bulk density of the complex nucleus increases with an increase in Ti content, and the average diameter decreases as the Nb content increases. Combined with the results in Section III-B, the above phenomenon could be attributed to the pinning effect of the Nb-rich outermost layer toward the complex nucleus, or the formation hysteresis of the complex nucleus because of the decrease in Ti content. However, in the two ingot types, the change in complex nucleus bulk density is obvious, and the influences of Ti content and solidification conditions are worth further studying.

IV. DISCUSSIONS

A. Solidification Characteristics and Formation of Complex Nucleus

The equilibrium phase during solidification of Fe-18 pct Cr FSS in this study was calculated by using Thermo-Calc equipped with the TCFE7 database according to the composition in Table I. The calculated phases in the range of 1400 °C to 1600 °C are shown in Figure 5.

In blank Ingots A and B, the equilibrium phases are liquid, δ-Fe, and silicon oxide. The Nb content in the silicon oxide of Ingot B is within 1.5 at. pct. When Ti was added to Ingots C and D, the oxide phase converted to TiO_x from the beginning of the melting stage, and an equilibrium phase with a NaCl-type face-centered cubic (FCC) structure appears during solidification. The NaCl-type phase in Ingot C represents Ti(C, N). When Nb is alloyed in Ingot D, the NaCl-type phase represents (Ti, Nb)_x(C, N)_y. Regardless of the presence of silicon oxide or TiO_x, the oxide has already formed during solidification in all four experimental Ingots. However, the NaCl type appeared only in the Ti-bearing phase of Ingots C and D during the solidification interval. The calculation results are consistent with the experimental results in Figure 3, which shows that it is thermodynamically feasible for silicon oxide or complex nucleus to form during solidification.

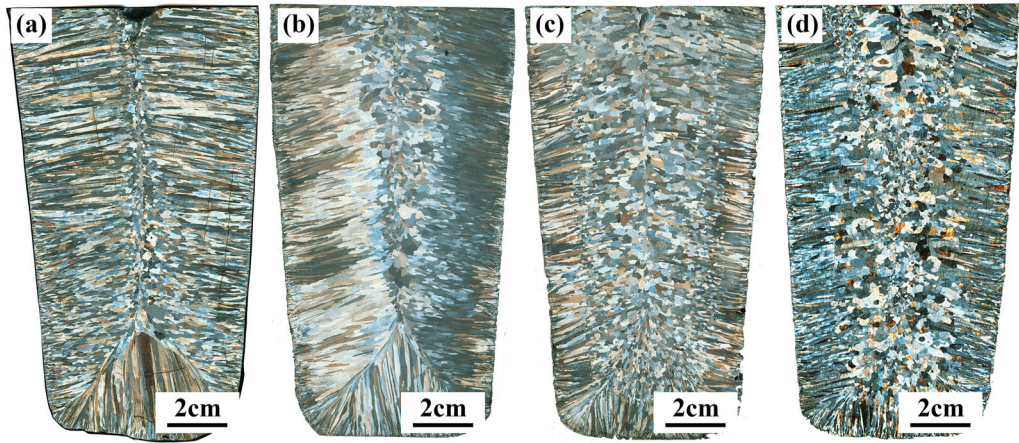


Fig. 2—Solidification structure of four ingots. (a) Ingot A with no Ti and Nb addition, (b) Ingot B with 0.20 mass pct Nb, (c) Ingot C with 0.16 mass pct Ti, and (d) Ingot D with 0.14 mass pct Ti and 0.21 mass pct Nb.

Although the formation of the complex nucleus has been explained, the formation mechanism of the third layer in the Nb-bearing layer remains unclear. Therefore, the Scheil-cooling model with segregation during solidification was applied to investigate this phenomenon. After considering the composition of Ingot D, the calculation results are shown in Figure 6.

The range of f_s (fraction of solid) from 0.9 to 0.98 and from 0.98 to 0.99 is enlarged in Figure 6 to facilitate observation. The solidification process can be divided into three stages. In stage 1, before solidification and with a solids fraction between 0 and 0.412, titanium oxide with a circular black shape is generated. In stage 2, with a solids fraction between 0.412 and 0.98, Ti-rich $(\text{Ti, Nb})_x(\text{C, N})_y$ will be generated on the surface of existing titanium oxide. In stage 3, with a solids fraction above 0.98, a Nb-rich layer will be generated to form an outermost layer, which could prevent the complex nucleus from growing and influence the reduction of inclusion size in the Ti and Nb-bearing Ingot D significantly.

The thermodynamic analysis indicates that a small amount of Ti can generate TiO_x . The experiment showed a good bonding ability between titanium oxide and $\text{Ti}(\text{C, N})$ or $(\text{Ti, Nb})_x(\text{C, N})_y$. Therefore, it is necessary to understand the oxide evolution and nucleation effect of TiO_x on $\text{Ti}(\text{C, N})$ or $(\text{Ti, Nb})_x(\text{C, N})_y$.

B. Oxide Evolution in Complex Nucleus with Ti Content

The addition of Ti converts the oxide from silicon oxide to TiO_x . Aluminum, which is a stronger deoxidizing element, could influence the oxide composition significantly. Although a certain amount of aluminum is present in the ingot, as shown in Table I, aluminum does not exist in the complex nucleus according to the EDS analysis. The Ti content and temperature have a significant influence on the type of TiO_x . Several compounds exist for TiO_x , such as Ti_2O_3 , Ti_3O_5 , TiO_2 , and TiO , where the structure has a significant influence on the formation of TiN and $\delta\text{-Fe}$.^[37–39]

The statistical results show that a small reduction of Ti in Ingot D leads to a significant reduction in the bulk density of the complex nucleus compared with Ingot C. Therefore, it is necessary to study the influence of elemental Ti and Al on the oxide types at the melting stage and during solidification.

The equilibrium phase diagrams with different Al, Ti, and O contents of Fe-18 pct Cr FSS at 1600 °C, 1550 °C, and 1510 °C were analyzed using FactSage 7.1 software, with the results being shown in Figure 7. Within the Ti content ranging from 0.001 to 1 mass pct and Al ranging from 1 mass ppm to 1 mass pct, four equilibrium oxides existed, namely Al_2O_3 , Ti_2O_3 , Ti_3O_5 , and liquid oxide. The boundary between the stable Al_2O_3 , Ti_2O_3 , and Ti_3O_5 phases are indicated by solid lines. The right side of the phase diagram is the stable phase region of Al_2O_3 , whereas the left represents Ti_2O_3 and Ti_3O_5 , and is separated by a horizontal solid line with a critical Ti content. The compositions of Ingots C and D are indicated by a solid circle and square, respectively. The stable phases in Ingots C and D are Ti_3O_5 at 1600 °C and 1550 °C. When the molten steel reaches 1510 °C, which is the temperature that precedes the solidification front, the stable oxide transformed from Ti_3O_5 to Ti_2O_3 in Ingot C, and Ti_3O_5 remained in Ingot D. The critical contents of Ti for the phase transformation of Ti_3O_5 and Ti_2O_3 are 0.226, 0.175, and 0.141 mass pct at 1600 °C, 1550 °C, and 1510 °C, respectively.

The critical content of Ti for phase transformation decreased as the temperature decreased. During solidification, the difference in temperature influences the type of critical Ti content for phase transformation between Ti_3O_5 and Ti_2O_3 significantly. Therefore, it is important to investigate the critical Ti content during cooling.

By using FactSage 7.1, the equilibrium phase diagram of the Ti-temperature system with different oxygen contents during solidification of Fe-18 pct Cr FSS was also calculated. Figure 8(a) shows the equilibrium phase with a Ti content from 0 to 1.0 mass pct, and a temperature ranging from 1200 °C to 1600 °C, where

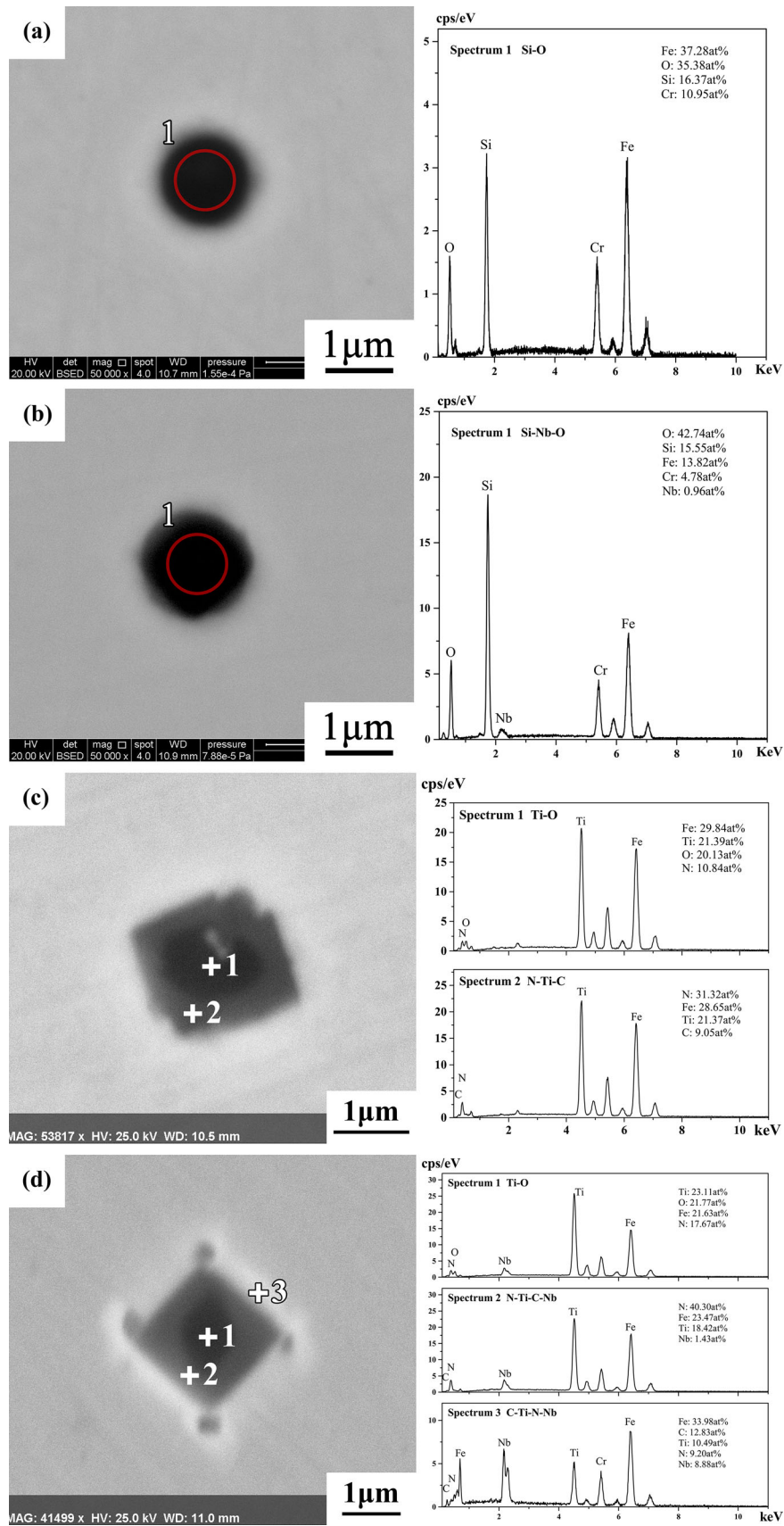


Fig. 3—Morphology and composition of major particles in the four ingots. (a) Si-O in Ingot A, (b) Si-Nb-O in Ingot B, (c) TiO_x-Ti(C, N) in Ingot C, and (d) TiO_x-(Ti, Nb)_x(C, N)_y in Ingot D.

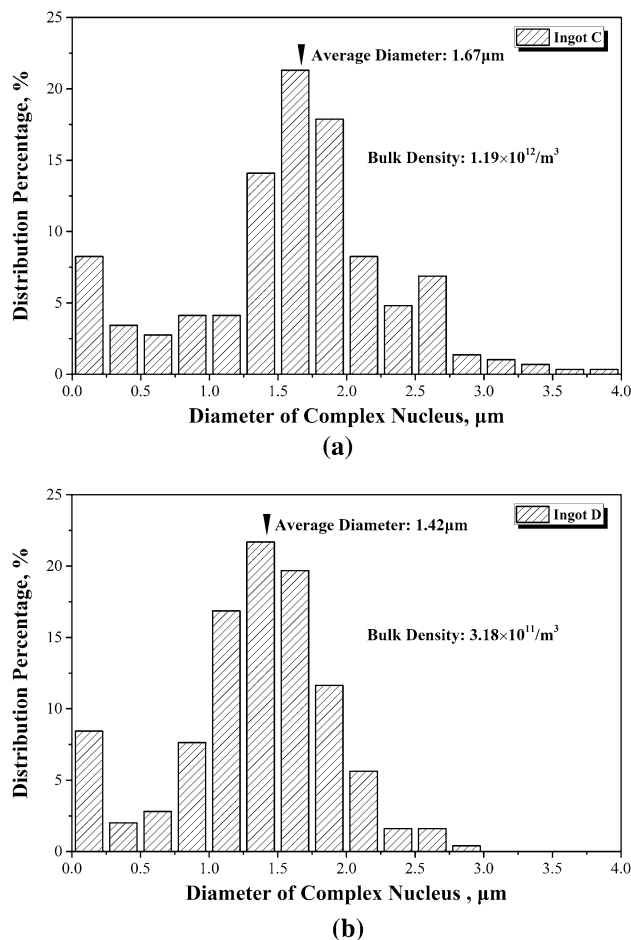


Fig. 4—Statistical analysis of complex nucleus in Ingots C and D. (a) Ingot C and (b) Ingot D.

AB, CD, AI, EFGH, and JKLM are the liquidus, solidus, TiO_x formation boundary, $(\text{Ti, Nb})_x(\text{C, N})_y$ formation boundary and phase boundary between Ti_2O_3 and Ti_3O_5 , respectively. Oxide evolution from 1450 °C to 1600 °C is detailed in Figure 8(b).

In Figure 8(b), the transformation boundary of Ti_3O_5 and Ti_2O_3 is indicated by a thick red solid line. The titanium-oxide formation boundary is represented by thin solid lines that are calibrated numerically with oxygen content. The Ti contents of Ingots C and D are indicated by dashed and dot-dashed lines, respectively. The equilibrium transformation boundary shows that the critical Ti content increases as the temperature increases, and the rate of increase is faster between the liquidus and solidus. The transformation relationship between the critical Ti and the temperature before solidification (above liquidus) can be expressed as shown in Eq. [1]:

$$[\text{mass pct Ti}] = 9 \times 10^{-4} \cdot \text{Temperature} - 1.22. \quad [1]$$

The transformation was completed before solidification in Ingot C, but occurred during solidification in Ingot D. If the presence of Ti_2O_3 can promote the formation of TiN and form the complex nucleus, then the decrease in bulk density of the complex nucleus in

Ingot D could be explained by this result. For the occurrence of CET, the transformation should be completed before solidification (above the liquidus). Therefore, the nucleation effects of Ti_3O_5 and Ti_2O_3 on $(\text{Ti, Nb})_x(\text{C, N})_y$ were discussed by disregistry theory to establish the optimal type of titanium oxide.

C. Effects of Ti_3O_5 and Ti_2O_3 on $(\text{Ti, Nb})_x(\text{C, N})_y$ Formation

For the disregistry calculations, it is important to establish the lattice structure of the relevant substances. Therefore, the three-dimensional lattice structures of Ti_3O_5 and Ti_2O_3 , and the TiN and atomic distribution in the low-index planes are shown in Figure 9. Because of the structural complexity of Ti_3O_5 , the atomic distributions in the (0 1/2 0) and (0 1 0) planes are listed in Figures 9(e) and (g), respectively. According to the coordination condition of chemical bonds in the molecule, schematic diagrams of the atomic distribution used in the disregistry calculation are shown in Figures 9(c), (d), and (h). The disregistry calculation model is described in detail elsewhere.^[40,41] The lattice system and parameters of the relevant substrate and nucleated solid are listed in Table II.^[40] Owing to the structural similarity, Ti(C, N) or $(\text{Ti, Nb})_x(\text{C, N})_y$ were considered as TiN, TiC, NbN, and NbC to simplify the calculation when they act as a substrate.

Figure 10 shows the orientation relationship between Ti_2O_3 , Ti_3O_5 , $\delta\text{-Fe}$, and NaCl-type FCC structure substrate, referring to TiN, TiC, NbN and NbC. The disregistry results are listed in Table III.

Bramfitt proposed that a substrate is effective in promoting the nucleation of a nucleated solid when the disregistry result is less than ~12 pct. According to Table III, the plane disregistry between Ti_2O_3 and TiN, TiC, NbC, NbN is less than 9 pct. However, the plane disregistry between Ti_3O_5 and TiN, TiC, NbC, NbN exceeds 12 pct. Therefore, $(\text{Ti, Nb})_x(\text{C, N})_y$ is more likely to be promoted by Ti_2O_3 . As mentioned in Section IV-B, Ti_2O_3 is more likely to be converted form Ti_3O_5 in Ingot C, because the transformation temperature is higher with 0.16 mass pct Ti. Therefore, Ti(C, N) is easier to be promoted to form the complex nucleus, which is consistent with the statistics. The disregistry values between $\delta\text{-Fe}$ and TiN, TiC, NbC, NbN are less than 9 pct, which indicates that $\delta\text{-Fe}$ will be effectively nucleated when $(\text{Ti, Nb})_x(\text{C, N})_y$ exists.

D. CET and As-cast Structure Variation Interacted with Nuclei Density and Dendritic Growth with Different Ti and Nb Contents

Although the nuclei density of Ingot D decreases significantly, the EZR of Ingot D is close to that of Ingot C, and the grain size of Ingot D is smaller. The as-cast structure provides a comprehensive result of nucleation and dendritic growth. For the Ti-bearing and Ti, Nb dual-stabilized FSS, the interaction effect of nuclei density and dendritic growth on the as-cast structure variation became more complicated, which is rarely mentioned in FSS.

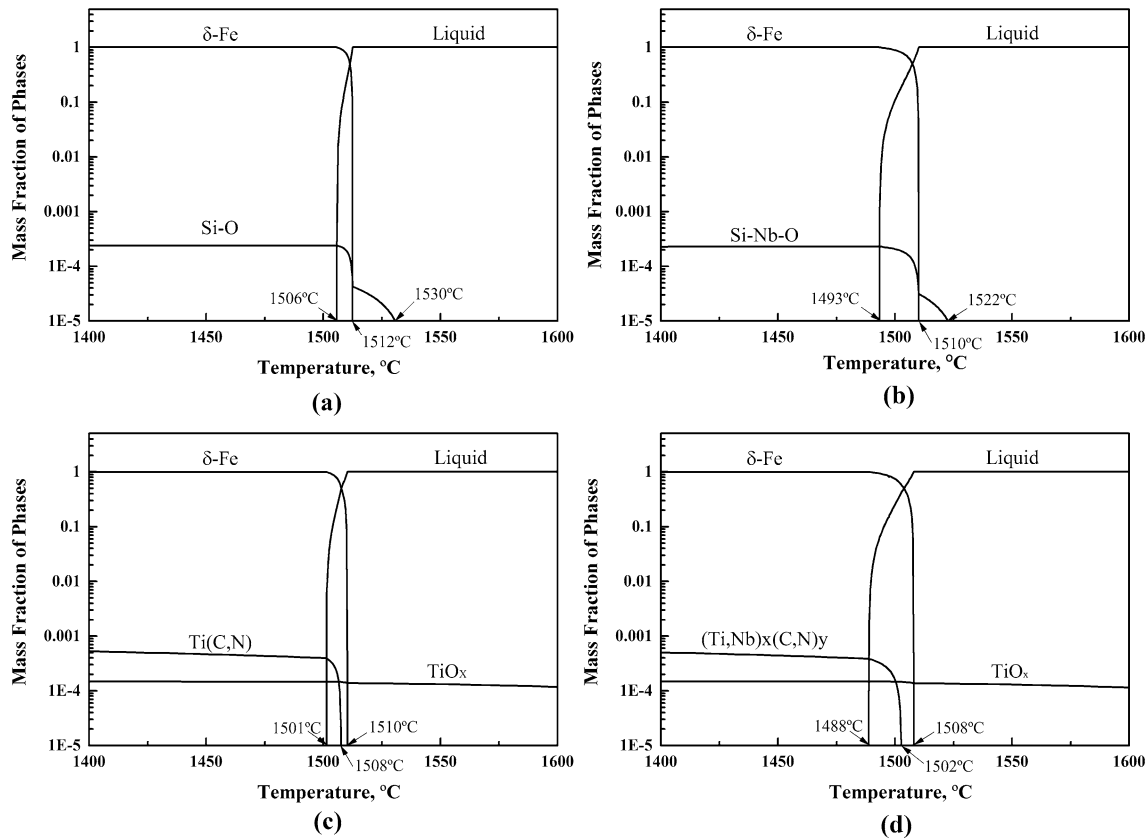


Fig. 5—Thermodynamics analysis during solidification and cooling. (a) Ingot A, (b) Ingot B, (c) Ingot C, and (d) Ingot D.

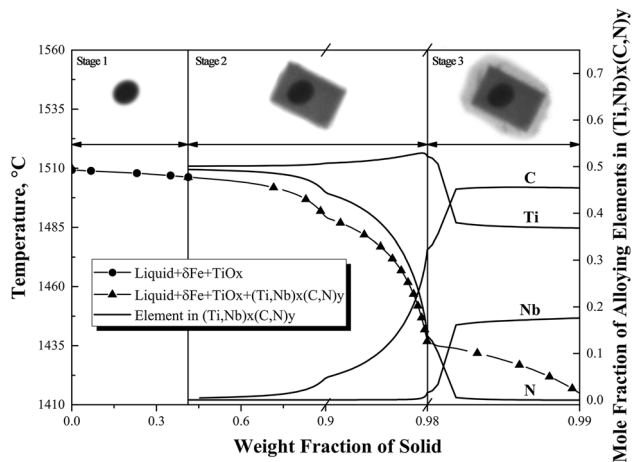


Fig. 6—Formation mechanism of three-layer complex nucleus in Ingot D.

The dendritic growth of the experiment ingots will be discussed as in previous work.^[11] The thermodynamic data, listed in Table IV, were calculated by using Thermo-Calc software with dendritic-growth-kinetic analysis involving a Fe-Cr-Ti-Nb-C-N six-component system in this study.

After solving the growth-kinetic equation numerically,^[11] the kinetic results are shown in Figure 11. The growth kinetics of Ingots A, B, C, and D are represented by dotted, dashed, dot-dashed, and solid lines, respectively. According to Figure 11, the growth-kinetic equations for Ingots A, B, C, and D can be expressed as Eqs. [2], [3], [4], and [5], respectively:

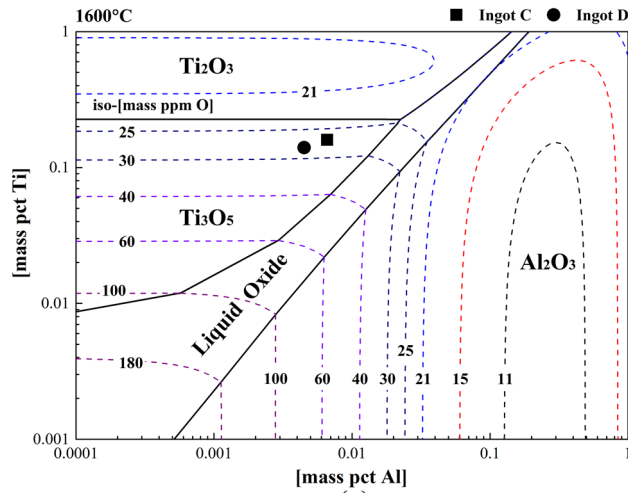
$$V_A = 1.89 \times 10^{-5} \cdot \Delta T^{3.86}, \quad [2]$$

$$V_B = 3.18 \times 10^{-6} \cdot \Delta T^{3.54}, \quad [3]$$

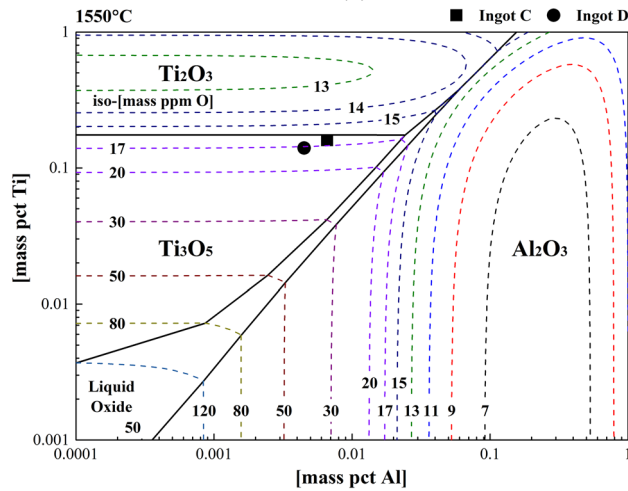
$$V_C = 1.18 \times 10^{-6} \cdot \Delta T^{4.13}, \quad [4]$$

$$V_D = 6.49 \times 10^{-7} \cdot \Delta T^{3.76}. \quad [5]$$

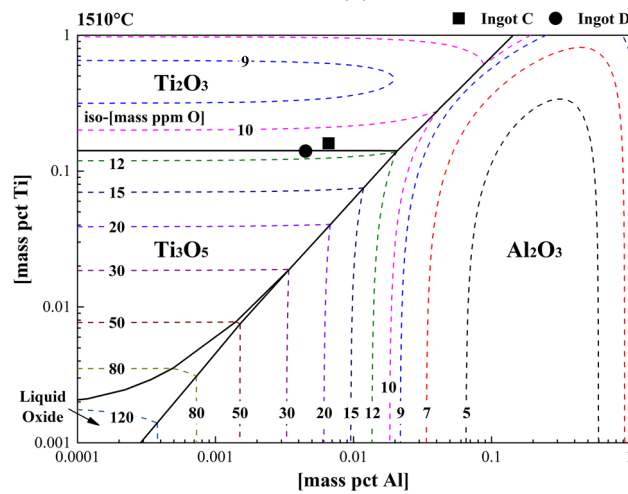
When Ti and Nb were alloyed, the slope of the growth-kinetic curve decreases, which indicates a lower growth velocity under the same undercooling conditions, which could lead to a smaller grain size. A larger dendrite tip undercooling could occur for the same



(a)

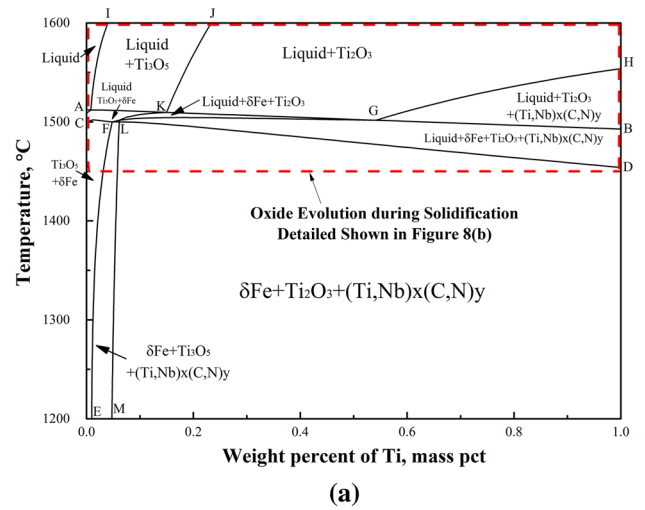


(b)

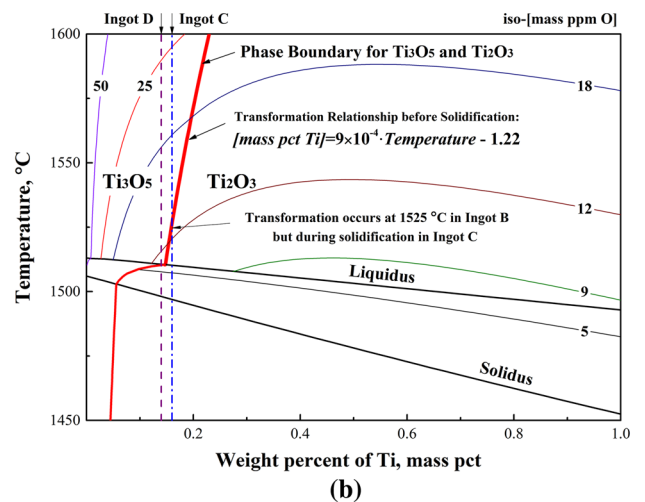


(c)

Fig. 7—Computed equilibrium phase diagram with different Al, Ti, and O contents in the Fe-18 mass pct Cr FSS at different temperatures; solid squares represent Ingot C, and solid circles represent Ingot D. (a) 1600 °C, (b) 1550 °C, and (c) 1510 °C.



(a)



(b)

Fig. 8—Computed stability diagram of phases and isolines [O] in Fe-18 mass pct Cr FSS with Ti content and temperature as variables. (a) Ti-temperature phase diagram and (b) oxide evolution with different initial oxygen contents, the phase boundary of $(\text{Ti, Nb})_x(\text{C, N})_y$ is hidden.

growth velocity, which provides suitable conditions for homogeneous and heterogeneous nucleation, and which results in a higher EZR.

The elemental influence level on dendritic growth increases in the order of Ingot A, C, B and D. Theoretically, if the nucleation ability of the four ingots is similar, the EZR of Ingot D should be highest. According to the discussions in Section IV-B, the formation of an effective nucleus was influenced mainly by Ti content. The maximum nucleation density was $3.6 \times 10^{11}/\text{m}^3$ and $9.6 \times 10^{10}/\text{m}^3$ for Ingots C and D, respectively, after considering the complex nucleus bulk density and nucleation efficiency as mentioned in Section III-C.

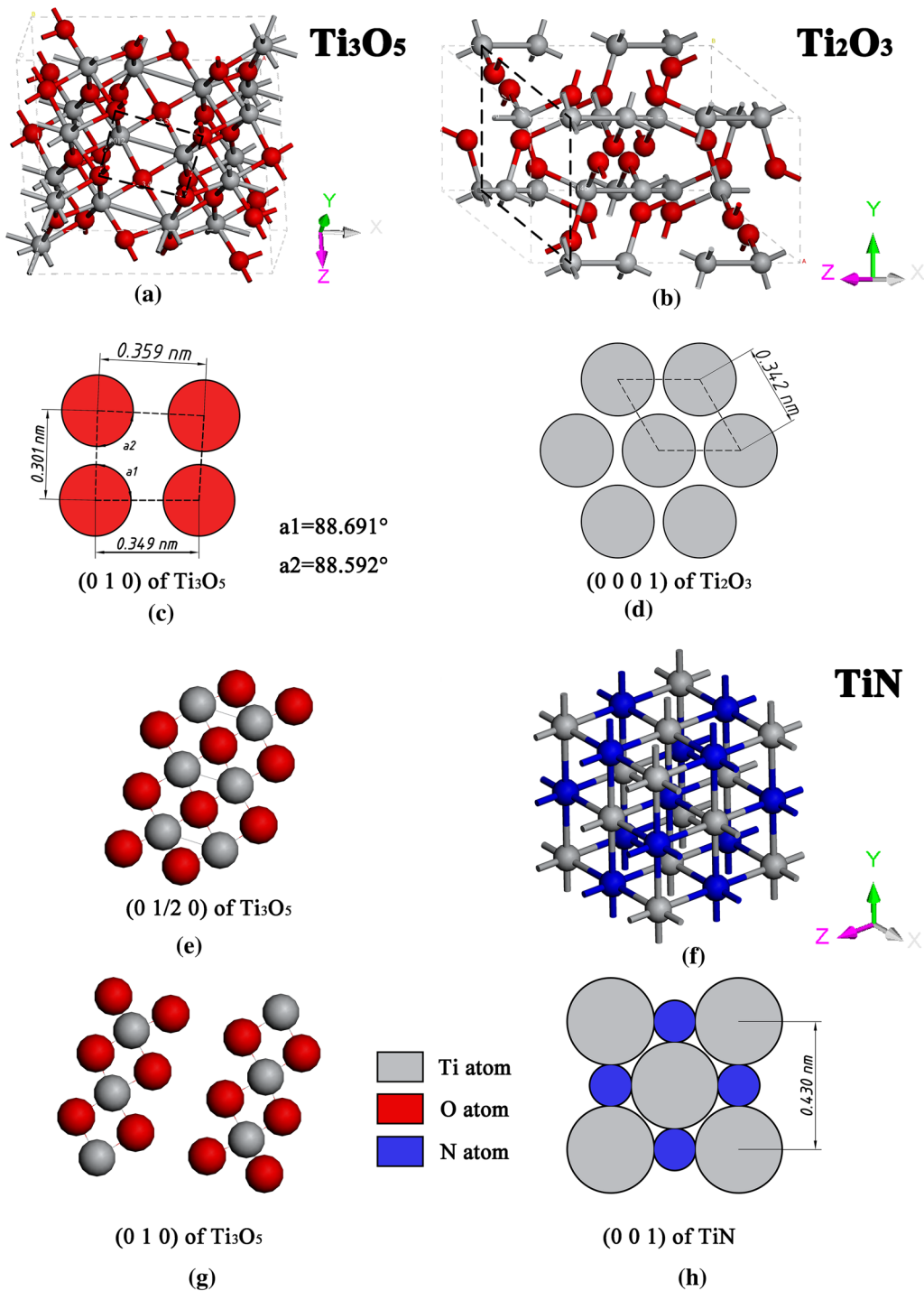


Fig. 9—Lattice structure of Ti_2O_3 , Ti_3O_5 and TiN . (a) Three-dimensional lattice structure of Ti_3O_5 , (b) three-dimensional lattice structure of Ti_2O_3 , (c) atoms in (010) plane of Ti_3O_5 , (d) atoms in (0001) plane of Ti_2O_3 , (e) (0 1/2 0) plane of Ti_3O_5 , (f) three-dimensional lattice structure of TiN , (g) (010) plane of Ti_3O_5 , and (h) atoms in (010) plane of TiN .

Table II. Lattice System and Parameters of Substrate and Nucleated Solid

Substance	$\delta\text{-Fe}$	Ti_2O_3	Ti_3O_5	NbC	NbN	TiC	TiN
Lattice	IM-3M	R-3C	C2/M	FM-3M	FM-3M	FM-3M	FM-3M
a_0 (nm)	0.294	0.513	9.7480	0.455	0.445	0.438	0.431

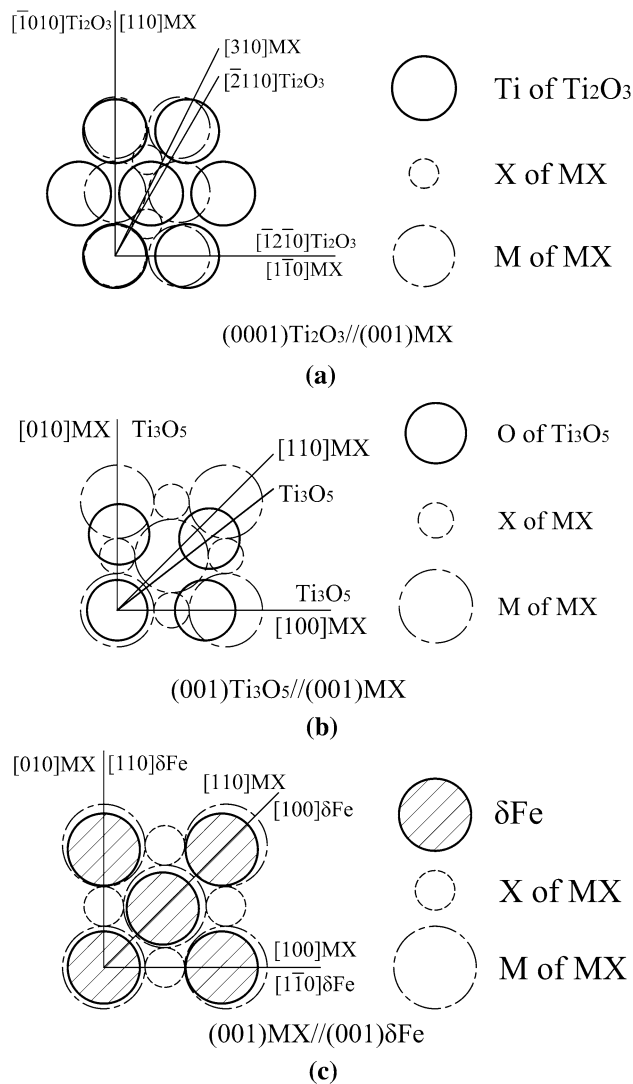


Fig. 10—Orientation relationship among Ti_2O_3 , Ti_3O_5 , MX and $\delta\text{-Fe}$, where MX refers to NaCl-type FCC structure carbonitride, M refers to Ti or Nb atoms, and X refers to C or N atoms. (a) Ti_2O_3 - MX , (b) Ti_3O_5 - MX , and (c) MX - $\delta\text{-Fe}$.

Table III. Disregistry Calculation Results (Percent)

	TiN	TiC	NbN	NbC
Ti_2O_3	5.12	5.40	5.83	6.46
Ti_3O_5	24.6	25.6	26.8	28.5
$\delta\text{-Fe}$	3.57	5.32	6.98	8.69

To explain the interaction influences on the EZR more clearly, a widely used CAFE model was used to illustrate the phenomenon combined with the nuclei density and dendritic growth data. The results are shown in Figure 12 with a comparison of the corresponding actual ingots.

The CET positions of the simulated result are consistent with those of an actual structure among the four ingots. Although the simulation results can better reflect the EZR of the experimental ingots, the equiaxed grains in the simulation results are much smaller than the actual ingot. This can be attributed to the fact that the CAFE model does not consider the merging and growth of grains at high temperatures after solidification, and these phenomena do occur in the FSS.^[43,44] By comparison, Nb addition can increase the EZR to some extent by slowing the dendritic growth. The EZR can be increased significantly owing to the formation of a large amount of complex nuclei when the Ti is alloyed in FSS, where the dendritic-growth-kinetic condition of Ingot C is similar to that of Ingot B according to Figure 11. When there are insufficient complex nuclei, the EZR will still decrease even if elemental Nb is alloyed in Ingot D compared with Ingot C. However, even if there are insufficient complex nuclei, the EZR of Ingot D is higher than that of Ingot B without complex nuclei.

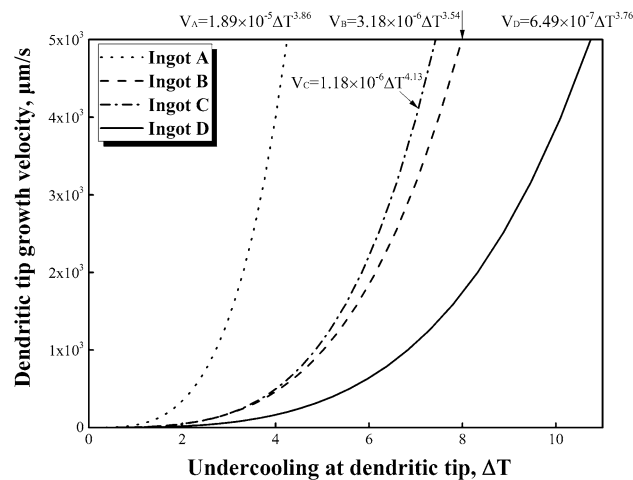


Fig. 11—Dendritic-growth kinetics of the four ingots.

Table IV. Data Used in Dendritic Growth-Kinetic Calculation

Parameters	Units	Cr	Ti	Nb	C	N
m_i	mass pct/K	- 0.34	- 19.27	- 13.1	- 95.3	- 78.3
k_i	—	0.99	0.34	0.20	0.16	0.28
D_{0_i} ^[42]	m ² /s	2.67×10^{-7}	1.81×10^{-7}	4.5×10^{-8}	1.43×10^{-7}	1.43×10^{-7}
Q_i ^[42]	J/mol	6.69×10^4	4.77×10^4	3.178×10^4	4.69×10^4	4.69×10^4

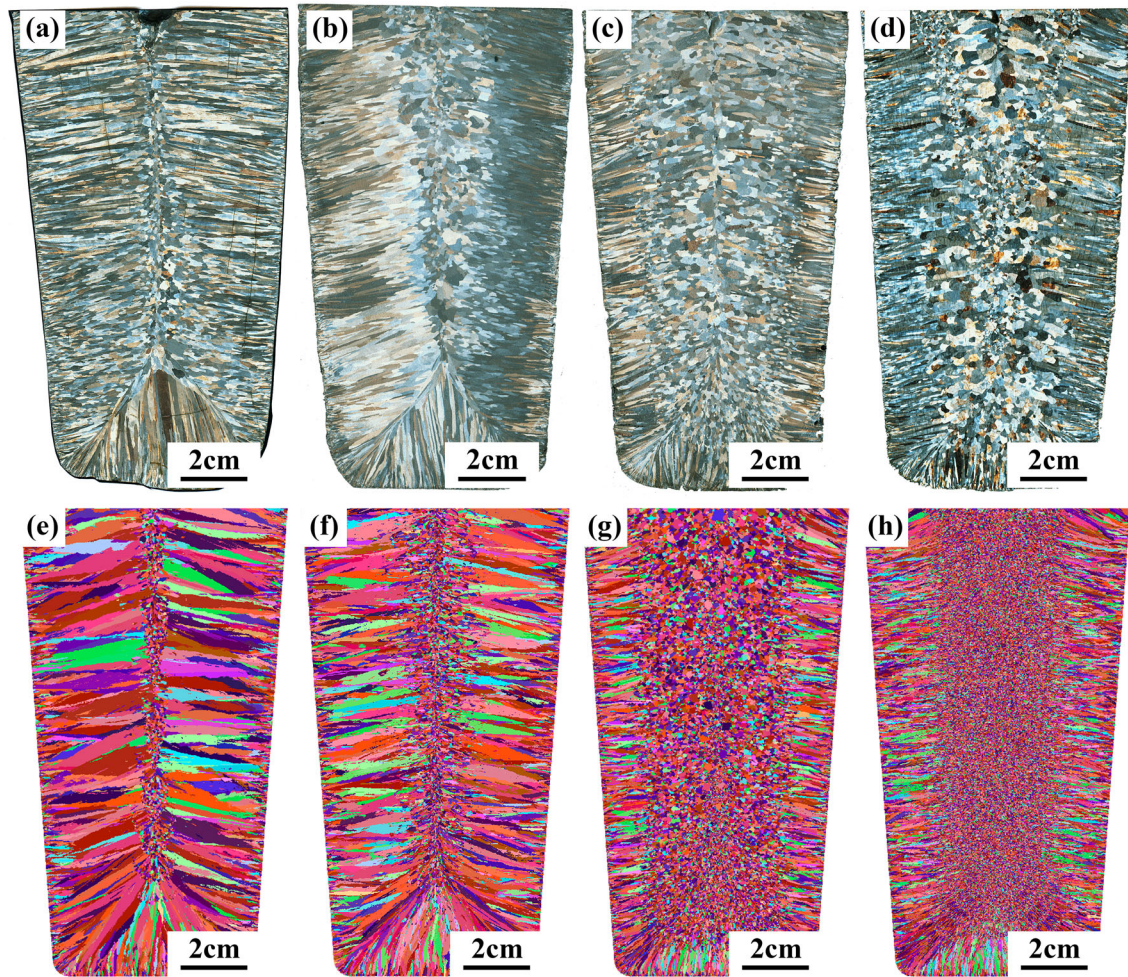


Fig. 12—Simulation and actual ingots with revealed structure in longitudinal section. (a), (b), (c), and (d) represent the actual as-cast structures of Ingots A, B, C, and D, respectively; and (e), (f), (g), and (h) represent the simulated structures of Ingots A, B, C, and D, respectively.

V. CONCLUSIONS

The interactive effect of nucleus density and dendritic growth on the solidification structure of Fe-18 pct Cr FSS was investigated.

1. The EZRs of blank Ingot A and Nb-bearing Ingot B were 8.5 and 28.8 pct, respectively, which indicates that Nb will increase the EZR slightly. When Ti was alloyed, the EZR increased to 67.5 and 57.3 pct in Ingots C and D, respectively, regardless of whether Nb was added or not. The grain size decreased as the Nb content increased.
2. The major inclusions are spherical silicon oxide in Ingots A and B. The major inclusions in Ingots C and D are mainly Ti-bearing complex nucleus. Statistics show that the bulk density of the complex nucleus of Ingot D decreased by 70 pct compared with Ingot C, when the Ti content decreased from 0.16 to 0.14 mass pct. The decrease may be attributed to a delay in phase transformation from Ti_3O_5 to Ti_2O_3 in the ingot with a lower Ti content, because Ti_2O_3 shows more potential for TiN formation compared with Ti_3O_5 according to the disregistry theory. The transformation relationship between the critical Ti

and the temperature before solidification can be expressed as $[Ti] = 9 \times 10^{-4} \cdot T - 1.22$.

3. The dendritic growth will be slowed when Ti or Nb is added to FSS, which will reduce the grain sizes and provide more opportunities for the formation of complex nuclei and the nucleation of δ -Fe, and result in an improved EZR. Modeling analysis shows that the dendritic growth equations for Ingots A, B, C, and D can be expressed as $V_A = 1.89 \times 10^{-5} \cdot \Delta T^{3.86}$, $V_B = 3.18 \times 10^{-6} \cdot \Delta T^{3.54}$, $V_C = 1.18 \times 10^{-6} \cdot \Delta T^{4.13}$, and $V_D = 6.49 \times 10^{-7} \cdot \Delta T^{3.76}$, respectively. CET transformation was illustrated after considering the nucleus density and growth kinetics with the CAFE method. The model results agree well with the actual CET positions of the four ingots. Because the growth velocity of the dendrite tip was slowed when alloying Ti and Nb, a similar EZR and finer grains are obtained even if the nucleation density of Ingot D is smaller than that of Ingot C. The nucleation effect is more obvious when the same amount of Ti or Nb is alloyed in FSS. Therefore, the amounts of alloying elements should be designated accordingly to obtain an appropriate EZR.

ACKNOWLEDGMENTS

This work was supported by the National Natural Science Foundation of China (Project Grant No. 51374020).

REFERENCES

1. H. Shin, J. An, S.H. Park, and D.N. Lee: *Acta Mater.*, 2003, vol. 51, pp. 4693–4706.
2. S. Park, K. Kim, Y. Lee, and C. Park: *ISIJ Int.*, 2002, vol. 42, pp. 100–05.
3. J. Hamada, Y. Matsumoto, F. Fudanoki, and S. Meada: *ISIJ Int.*, 2003, vol. 43, pp. 1989–98.
4. K. Kawahara: *J. Jpn. Inst. Met.*, 1974, vol. 38, p. 440.
5. P.D. Wu, H. Jin, Y. Shi, and D.J. Lloyd: *Mater. Sci. Eng. A*, 2006, vol. 423, pp. 300–05.
6. M.Y. Huh and O. Engler: *Mater. Sci. Eng. A*, 2001, vol. 308, pp. 74–87.
7. H. Chao: *Metall. Trans.*, 1973, vol. 4, pp. 1183–86.
8. R.N. Wright: *Metall. Mater. Trans. B*, 1972, vol. 3B, pp. 83–91.
9. J.C. Kim, J.J. Kim, J.Y. Choi, J.H. Choi, and S.K. Kim: *La Metall. Ital.*, 2009, vol. 101, pp. 43–48.
10. Y. Itoh, T. Okajima, and K. Tashiro: *Tetsu-to-Hagane*, 1980, vol. 66, pp. 1093–1102.
11. Y. Hou, S. Li, and G. Cheng: *Metall. Mater. Trans. A*, 2018, vol. 49A, pp. 5455–57.
12. B.L. Bramfitt: *Metall. Trans.*, 1970, vol. 1, pp. 1987–95.
13. Y. Itoh, S. Takao, T. Okajima, and K. Tashiro: *Tetsu-to-Hagane*, 1980, vol. 66, pp. 710–16.
14. X. Shi, G. Cheng, and P. Zhao: *J. Univ. Sci. Technol. B*, 2010, vol. 32, pp. 1277–81.
15. H. Fujimura, S. Tsuge, Y. Komizo, and T. Nishizawa: *Tetsu-to-Hagane*, 2001, vol. 87, pp. 707–12.
16. J.H. Park: *CALPHAD*, 2011, vol. 35, pp. 455–62.
17. N. Fujita, K. Ohmura, M. Kikuchi, T. Suzuki, S. Funaki, and I. Hiroshige: *Scripta Mater.*, 1996, vol. 35, pp. 705–10.
18. G.M. Sim, J.C. Ahn, S.C. Hong, K.J. Lee, and K.S. Lee: *Mater. Sci. Eng. A*, 2005, vol. 396, pp. 159–65.
19. P.R. Scheller, S. Lachmann, C. Klinkenberg, K. Hulka, and A. Weiss: *ISIJ Int.*, 2006, vol. 46, pp. 1865–70.
20. J.A. Spittle: *Int. Mater. Rev.*, 2006, vol. 51, pp. 247–69.
21. M. Gäumann, R. Trivedi, and W. Kurz: *Mater. Sci. Eng. A*, 1997, vol. 226, pp. 763–69.
22. H. Takeuchi, Y. Ikehara, T. Yanai, and S. Matsumura: *Trans. Iron Steel Inst. Jpn.*, 1978, vol. 18, pp. 352–60.
23. C.W. Bale, P. Chartrand, S.A. Decterov, G. Eriksson, K. Hack, R. Ben Mahfoud, J. Melançon, A.D. Pelton, and S. Petersen: *CALPHAD*, 2002, vol. 26, pp. 189–228.
24. C.W. Bale, E. Bélisle, P. Chartrand, S.A. Decterov, G. Eriksson, K. Hack, I.-H. Jung, Y.-B. Kang, J. Melançon, A.D. Pelton, C. Robelin, and S. Petersen: *CALPHAD*, 2009, vol. 33, pp. 295–311.
25. C.W. Bale, E. Bélisle, P. Chartrand, S.A. Decterov, G. Eriksson, A.E. Gheribi, K. Hack, I.-H. Jung, Y.-B. Kang, J. Melançon, A.D. Pelton, S. Petersen, C. Robelin, J. Sangster, P. Spencer, and M.-A. Van Ende: *CALPHAD*, 2016, vol. 54, pp. 35–53.
26. B. Sundman, B. Jansson, and J. Andersson: *CALPHAD*, 1985, vol. 9, pp. 153–90.
27. J. Andersson, T. Helander, L. Höglund, P. Shi, and B. Sundman: *CALPHAD*, 2002, vol. 26, pp. 273–312.
28. W. Kurz, B. Giovanola, and R. Trivedi: *Acta Mater.*, 1986, vol. 34, pp. 823–30.
29. W.W. Mullins and R.F. Sekerka: *J. Appl. Phys.*, 1964, vol. 35, pp. 444–51.
30. W. Kurz and D.J. Fisher: *Acta metall.*, 1981, vol. 29, pp. 11–20.
31. J. Lipton, M.E. Glicksman, and W. Kurz: *Metall. Trans. A*, 1987, vol. 18, pp. 341–45.
32. M. Rappaz and C.A. Gandin: *Acta metall.*, 1993, vol. 41, pp. 345–60.
33. P. Thévoz, L. Desbiolles, and M. Rappaz: *Metall. Trans. A*, 1989, vol. 20, pp. 311–22.
34. M. Rappaz: *Int. Mater. Rev.*, 1989, vol. 34, pp. 93–124.
35. C.A. Gandin, J.L. Desbiolles, M. Rappaz, and P. Thevoz: *Metall. Mater. Trans. A*, 1999, vol. 30A, pp. 3153–65.
36. J. Fu, Q. Nie, W. Qiu, J. Liu, and Y. Wu: *Mater. Charact.*, 2017, vol. 133, pp. 176–84.
37. J.S. Park and J.H. Park: *Steel Res. Int.*, 2014, vol. 85, pp. 1303–09.
38. A. Ito, H. Suito, and R. Inoue: *ISIJ Int.*, 2012, vol. 52, pp. 1196–1205.
39. S.K. Kim, H. Suito, and R. Inoue: *ISIJ Int.*, 2012, vol. 52, pp. 1935–44.
40. Y. Hou and G. Cheng: *ISIJ Int.*, 2018, vol. 58, pp. 2298–2307.
41. J.S. Park, C. Lee, and J.H. Park: *Metall. Mater. Trans. B*, 2012, vol. 43A, pp. 1550–64.
42. K. Kimura, S. Fukumoto, G. Shigesato, and A. Takahashi: *ISIJ Int.*, 2013, vol. 53, pp. 2167–76.
43. A. Belyakov, Y. Kimura, and K. Tsuzaki: *Mater. Sci. Eng. A*, 2005, vol. 403, pp. 249–59.
44. M. Aksoy, S.O. Yilmaz, and E. Evin: *Proc. Inst. Mech. Eng.*, 2009, vol. 223, pp. 39–49.

Publisher's Note Springer Nature remains neutral with regard to jurisdictional claims in published maps and institutional affiliations.